PHYSICS OF FLUIDS **25**, 055107 (2013)

Turbulent premixed combustion in V-shaped flames: Characteristics of flame front

S. Kheirkhah[a] and Ö. L. Gülder
University of Toronto Institute for Aerospace Studies, Toronto, Ontario M3H 5T6, Canada

(Received 6 December 2012; accepted 1 May 2013; published online 31 May 2013)

Flame front characteristics of turbulent premixed V-shaped flames were investigated experimentally using the Mie scattering and the particle image velocimetry techniques. The experiments were performed at mean streamwise exit velocities of 4.0, 6.2, and 8.6 m/s, along with fuel-air equivalence ratios of 0.7, 0.8, and 0.9. Effects of vertical distance from the flame-holder, mean streamwise exit velocity, and fuel-air equivalence ratio on statistics of the distance between the flame front and the vertical axis, flame brush thickness, flame front curvature, and angle between tangent to the flame front and the horizontal axis were studied. The results show that increasing the vertical distance from the flame-holder and the fuel-air equivalence ratio increase the mean and root-mean-square (RMS) of the distance between the flame front and the vertical axis; however, increasing the mean streamwise exit velocity decreases these statistics. Spectral analysis of the fluctuations of the flame front position depicts that the normalized and averaged power-spectrum-densities collapse and show a power-law relation with the normalized wave number. The flame brush thickness is linearly correlated with RMS of the distance between the flame front and the vertical axis. Analysis of the curvature of the flame front data shows that the mean curvature is independent of the experimental conditions tested and equals to zero. Values of the inverse of the RMS of flame front curvature are similar to those of the integral length scale, suggesting that the large eddies in the flow make a significant contribution in wrinkling of the flame front. Spectral analyses of the flame front curvature as well as the angle between tangent to the flame front and the horizontal axis show that the power-spectrum-densities feature a peak. Value of the inverse of the wave number pertaining to the peak is larger than that of the integral length scale. © *2013 AIP Publishing LLC*. [http://dx.doi.org/10.1063/1.4807073]

I. INTRODUCTION

Turbulent premixed combustion is the mode of operation in several industrial combustion systems such as, stationary gas turbines, lean premixed and prevaporized jet engines, and spark ignition engines.[1–3] Since a comprehensive understanding of physics and chemistry involved in turbulent premixed combustion directly benefits operation of several types of combustion equipment, experimental, theoretical, and numerical research in this area have been performed during the last decades (see, for example, the review papers by Clavin,[3] Driscoll,[4] and Lipatnikov and Chomiak[5]). A survey of literature shows that flame configurations investigated in previous studies are mainly V-shaped, spherical, conical, or stagnant. The flame configuration investigated in the present study is V-shaped. Motivation for this study is twofold. First, the experimental results presented in this article are utilized as a benchmark for future numerical simulations. The combined numerical and experimental research will be used to develop models for simulating combustion in gas turbine engines. Second, although a large body of research has been devoted to investigate turbulent premixed combustion in V-shaped flames, yet several flame front characteristics, e.g., flame front curvature

[a]Electronic mail: kheirkhah@utias.utoronto.ca

and orientation, are not studied in detail. Findings of the past investigations associated with the flame front characteristics, specifically, flame front position, flame brush thickness, and flame front curvature are presented below.

Lipatnikov and Chomiak,[5] Shepherd *et al.*,[6] and Namazian *et al.*[7] investigated mean, root-mean-square (RMS), and probability-density-function (PDF) of flame front position (x), i.e., the distance between the flame front and the vertical axis, in V-shaped flames. Results presented by Lipatnikov and Chomiak[5] indicate that the mean of the distance between the flame front and the vertical axis ($\overline{x}$) increases by increasing the vertical distance from the flame-holder (y). Discussions presented by Lipatnikov and Chomiak[5] and Shepherd *et al.*[6] show that the RMS of the distance between the flame front and the vertical axis (x') is significantly dependent on the vertical distance from the flame-holder, the fuel-air equivalence ratio (ϕ), and the turbulence intensity in the reactants flow (u'/S_L), where u' and S_L are the RMS of streamwise velocity in unburnt gas and the laminar flame speed, respectively. Previous studies[5,6] show that increasing the vertical distance from the flame-holder increases the RMS of the flame front position. Also, at a fixed vertical distance from the flame-holder and for lean flame conditions, increasing the fuel-air equivalence ratio, and the turbulence intensity, increase RMS of the flame front position. Further, experimental results[6,7] show that the probability-density-function of the flame front position has a Gaussian distribution.

The flame brush thickness (δ_t) is significantly dependent on the vertical distance from the flame-holder, mean (U), and RMS (u') of the streamwise velocity at the exit of the burner, integral length scale (Λ) measured in the reactants flow, and the fuel-air equivalence ratio.[5,7,8] Results of Lipatnikov and Chomiak[5] show that, relatively close to the flame-holder, the flame brush thickness is linearly correlated with y and u'/U, and is given by $\delta_t \approx yu'/U$. However, far away from the flame-holder, the flame brush thickness is proportional to the square roots of both the vertical distance from the flame-holder as well as u'/U and is given by $\delta_t \approx \sqrt{2\Lambda yu'/U}$. Although the mathematical formulations presented in Lipatnikov and Chomiak[5] do not show a dependance between the flame brush thickness and the fuel-air equivalence ratio, the experimental results presented in Namazian *et al.*[7] show that δ_t is significantly dependent on ϕ. Specifically, their results[7] show that, for lean combustion, increasing the fuel-air equivalence ratio increases the flame brush thickness.

Veynante *et al.*[9] and Soika *et al.*[10] investigated flame front curvature (κ) in turbulent premixed V-shaped flames. Their results indicate that, close to the reactants region, the flame front curvature is mostly positive, i.e., convex towards the reactants, and is accompanied by small local temperature gradient across the flame front. As a result, close to the reactants region, species diffusion and reaction rates are small.[9,10] However, close to the products region, the flame front curvature is mostly negative, i.e., concave towards the reactants region, and is accompanied by large temperature gradient across the flame front. Thus, the species diffusion and reaction rates are relatively large close to the products region.

Although previous investigations associated with turbulent premixed combustion in V-shaped flames have provided significant insight into several flame front characteristics, such as position of the flame front and flame brush thickness, few investigations have studied statistics of flame front curvature. The present study aims at first revisiting previous observations made for statistics of flame front position and flame brush thickness, then expanding on the current knowledge of statistics of flame front curvature as well as flame front orientation.

II. EXPERIMENTAL METHODOLOGY

This section consists of the experimental setup utilized to produce the V-shaped flame configuration, measurement techniques used to investigate the flame front characteristics, and the experimental conditions tested.

A. Experimental setup

Burner setup

The turbulent premixed V-shaped flames were produced using the setup presented in Fig. 1(a). The burner is composed of an expansion section, a settling chamber, a contraction section, a nozzle,

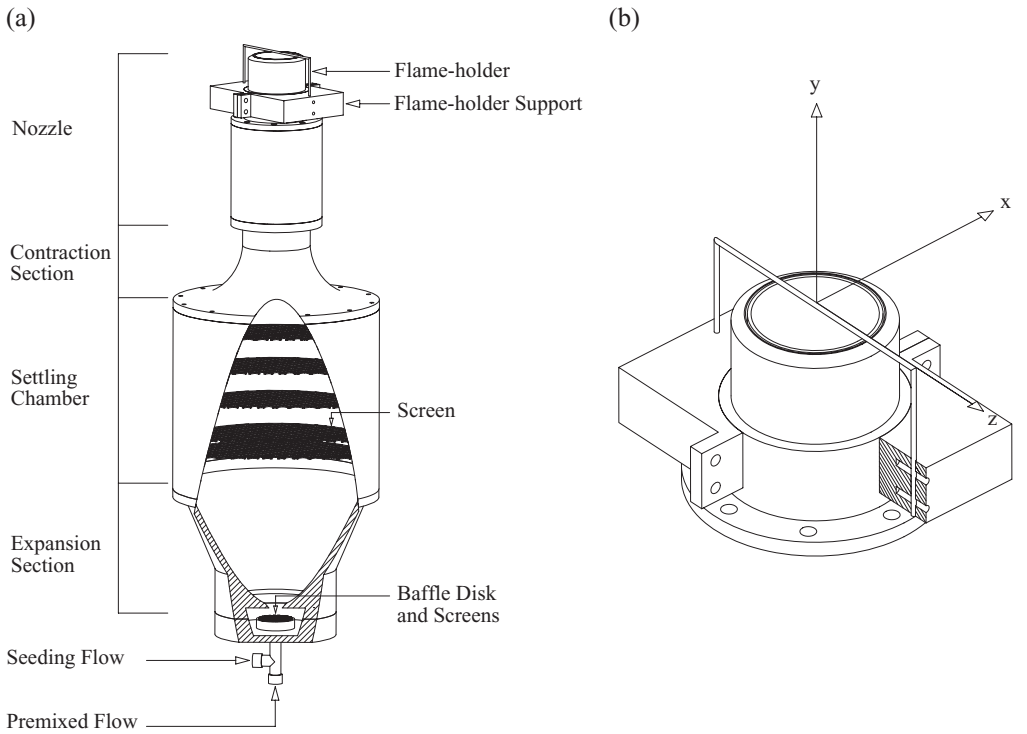

FIG. 1. (a) Burner setup and (b) flame-holder and flame-holder support details.

a flame-holder support, and a flame-holder. The expansion section has an expansion area ratio of about four. Close to the entrance of the expansion section, a baffle disk is placed in order to disperse the entering air-fuel mixture and the seeding flow (Fig. 1(a)). A settling chamber, equipped with five square-mesh screens, is installed after the expansion section for flow conditioning purposes (Fig. 1(a)). The settling chamber is followed by a contraction section with a contraction area ratio of approximately seven. After the contraction section, a nozzle with inner diameter (D) of 48.4 mm is placed. Turbulence generating apparatus can be installed inside the nozzle. A flame-holder, made of brass wire, is placed close to the exit of the nozzle (Figs. 1(a) and 1(b)). The wire diameter (d) is 2 mm. The wire is fixed using the flame-holder support, with details provided in Fig. 1(b). Parallel and circular guiding holes were generated on the flame-holder support. The guiding holes serve as a sliding mechanism which allows for adjusting the distance between the flame-holder centerline and the exit plane of the burner (Fig. 1(b)). This distance was fixed at 4 mm for all the experiments.

Coordinate system

The coordinate system utilized in the present investigation is Cartesian, as shown in Fig. 1(b). The origin of the coordinate system is located equidistant from both ends of the flame-holder, and 5 mm above the burner exit plane. The y-axis of the coordinate system is normal to the exit plane of the burner. The x-axis is normal to both y-axis and the flame-holder centerline. The z-axis is normal to both x and y axes and lies along the span of the flame-holder.

Turbulence generating mechanism

A stainless steel perforated plate, with technical drawing provided in Fig. 2(a), was utilized for turbulence generation purposes. The plate had an outer diameter (D) of 48.4 mm and a thickness (t) of 1 mm. Sixty seven circular holes were generated on the plate. The holes were arranged in a hexagonal pattern (Fig. 2(a)). The hole diameter (D_h) was 3.9 mm, and the distance between each two neighboring holes (s) was 5.7 mm. The plate blockage ratio ($B = 1 - A_h/A_t$) was 58%, where A_h

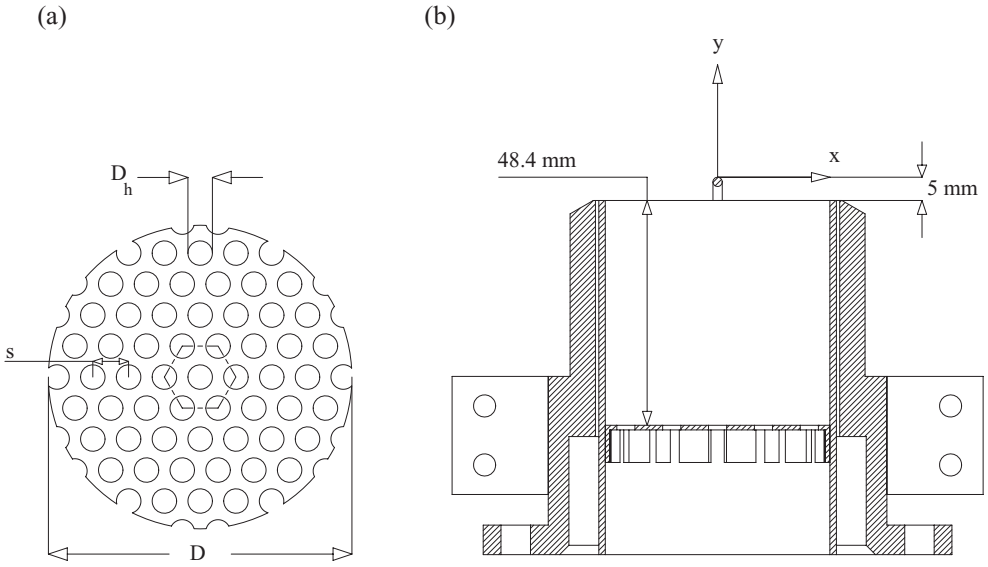

FIG. 2. (a) Perforated plate and (b) plate arrangement inside the burner nozzle.

and A_t are the area of the holes and the total area of the plate, respectively. Details of the geometrical dimensions of the plate are provided in Table I.

The turbulence generating plate was located 48.4 mm upstream of the nozzle exit plane, as shown in Fig. 2(b). The rim of the plate was bent in order to provide a contact region between the plate and the inner surface of the nozzle (Fig. 2(b)). This allowed for precise positioning of the plate inside the nozzle, such that the plate remained parallel with the exit plane of the burner during the experiments.

B. Measurement techniques

Mie scattering

The Mie scattering technique was utilized to study the flame front characteristics. As defined by Eckbreth,[11] the Mie scattering is elastic scattering of light, with wave length λ, from particles with average size d_p, when $d_p \gtrsim \lambda$. The Mie scattering technique is widely used in the past studies[12–19] for investigation of characteristics of V-shaped flames. An underlying assumption in application of the Mie scattering technique for studying flame front characteristics is that combustion occurs inside a relatively thin layer.[18,19] This assumption is called the flamelet assumption.[20] Implication of the flamelet assumption is that if the reactants are seeded with particles which evaporate at the flame front, the light intensities scattered from the particles inside the reactants region will be significantly larger than those inside the products region. This marked difference in the light intensities is utilized for detection of the flame front.[17–19] A Laskin-nozzle type nebulizer, previously used in the studies of Smallwood *et al.*,[21] Gülder,[22] and Yuen,[23] was utilized for seeding purposes in the Mie scattering experiments. The olive oil droplets, which have been previously assessed to be proper for Mie scattering experiments in the past investigations,[17,24] were utilized in the present study.

TABLE I. Perforated plate geometrical dimensions.

D	48.4 mm
D_h	3.9 mm
s	5.7 mm
t	1 mm

The Mie scattering is a two-dimensional imaging technique. Since the flame surfaces investigated in the present study may be three-dimensionally oriented, one may argue that the two-dimensional measurements are not capable of capturing the flame front characteristics. However, while performing two and three-dimensional measurements, Chen *et al.*[25] demonstrated that the characteristics of flame surfaces associated with both types of measurements are very similar. Further, due to the specific geometry of V-shaped flames, and isotropy arguments, it is believed that the planar measurements would capture the essential characteristics of V-shaped flames.

The hardware associated with the Mie scattering technique consists of a CCD camera and a Nd:YAG pulsed laser. The camera has a resolution of 2048 pixels × 2048 pixels. The camera head is equipped with a macro Sigma lens, which has a focal length (f) of 105 mm. During the experiments, the lens aperture size was fixed at $f/8$. In order to avoid influence of flame chemiluminescence in acquired images, the lens was equipped with a 532 nm band-pass filter. For all the experiments, imaging field of view was 60 mm × 60 mm.

The flow field was illuminated by a laser sheet formed from a 6.5 mm diameter beam, which has a wavelength of 532 nm, a beam energy of about 120 mJ per pulse, and a pulse duration of about 4 ns. At the plane of $z/d = 0$, where all the experiments were performed, the laser sheet thickness was measured to be 150 ± 50 μm. The laser operated at a frequency of 5 Hz and the Mie scattering images were simultaneously acquired by the CCD camera. For statistical analysis of the flame front characteristics, 1000 images were acquired for each experimental condition tested.

The recorded images were binarized using a threshold-based technique. The binarization process is usually accompanied by digitization noise.[26] In order to reduce the noise, a median-finding-based algorithm was utilized to filter the binarized images. The filter size was selected to be equal to the inner cutoff scale[26] (ϵ_i). The value of the inner cutoff scale was estimated from $\epsilon_i = 7\delta_L Ka^{-1/2}$ proposed by Roberts *et al.*,[27] where δ_L and Ka are the laminar flame thickness and the Karlovitz number, respectively. Depending on the experimental condition tested, value of ϵ_i was varied between 0.5 mm and 1 mm. After filtering the binarized images, the contour algorithm in MATLAB was used to obtain the flame front.

Particle image velocimetry

The Particle Image Velocimetry (PIV) technique was utilized to measure turbulent flow characteristics. The PIV images were acquired for non-reacting flow condition and without the flame-holder. The PIV hardware is identical to that utilized for the Mie scattering experiments. All the PIV experiments were performed at the plane of $z/d = 0$. For each experimental condition tested, 1000 image pairs were acquired at a frequency of 5 Hz. For velocity data analysis, the interrogation box size was selected to be 16 pixels, with zero overlap between the boxes. For each experimental condition, the separation time between the laser pulses was selected such that the average distance traced by the seeding particles in each interrogation box was approximately 25% of the size of each interrogation box. This was performed in order to avoid particles loss between consecutive images. Olive oil droplets were used for seeding in the PIV experiments. These droplets were assessed to be proper for the flow seeding based on the particles Stokes number. For all experimental conditions tested, the Stokes number of the olive oil droplets was estimated to be smaller than 0.01. This indicates that the droplets are proper for flow seeding in the PIV experiments.

C. Experimental conditions

The tested experimental conditions are tabulated in Table II. Methane grade 2, i.e., methane with 99% chemical purity, was used as the fuel in the experiments. Three mean streamwise exit velocities ($U = 4.0$, 6.2, and 8.6 m/s) were examined in the experiments. Mean and RMS of the exit velocities were estimated at $x/d = 0$, $y/d = -1$, and $z/d = 0$ (see Fig. 1(b)). For each mean streamwise exit velocity, three fuel-air equivalence ratios were tested ($\phi = 0.7$, 0.8, and 0.9). The laminar flame speed and the laminar flame thickness were obtained from the data provided by Andrews and Bradley[28] and Jarosinski,[29] respectively. For each experimental condition, the integral length scale was estimated using the streamwise velocity autocorrelation[30] calculated along the y-axis. The Kolmogorov length

TABLE II. Tested experimental conditions.

	Symbol	U(m/s)	u'(m/s)	v'(m/s)	ϕ	S_L(m/s)	δ_L(mm)	η(mm)	Λ(mm)	Re_Λ	Ka	Da
Flame A	○	4.0	0.27	0.25	0.7	0.23	0.22	0.14	2.1	35.5	2.5	8.1
Flame B	□	4.0	0.27	0.25	0.8	0.30	0.17	0.14	2.1	35.5	1.5	13.7
Flame C	◇	4.0	0.27	0.25	0.9	0.37	0.14	0.14	2.1	35.5	1.0	20.6
Flame D	×	6.2	0.51	0.38	0.7	0.23	0.22	0.09	1.9	60.6	6.0	3.9
Flame E	+	6.2	0.51	0.38	0.8	0.30	0.17	0.09	1.9	60.6	3.6	6.6
Flame F	✱	6.2	0.51	0.38	0.9	0.37	0.14	0.09	1.9	60.6	2.4	9.8
Flame G	△	8.6	0.62	0.51	0.7	0.23	0.22	0.08	2.3	89.2	7.6	3.9
Flame H	◁	8.6	0.62	0.51	0.8	0.30	0.17	0.08	2.3	89.2	4.5	6.5
Flame I	▷	8.6	0.62	0.51	0.9	0.37	0.14	0.08	2.3	89.2	3.1	9.8

scale (η) was obtained from $\eta = \Lambda Re_\Lambda^{-3/4}$. In Table II, the Reynolds, Karlovitz, and Damköhler numbers were calculated from $Re_\Lambda = u'\Lambda/\nu$, $Ka = (\delta_L/\eta)^2$ and $Da = S_L\Lambda/u'\delta_L$, respectively. The experimental conditions of the flames tested in the present investigation are overlaid on the premixed combustion regime diagram, presented in Fig. 3. The experimental conditions were selected such that the corresponding data points on the diagram pertain to wrinkled flames, corrugated flames, and thin reaction zones.

III. RESULTS

A. Flame front position

A representative Mie scattering image corresponding to Flame A is presented in Fig. 4(a). As shown in the figure, the flame front is composed of two edges. The edge that is located on the right-hand-side of Fig. 4(a) is referred to as the right wing, and that located on the left-hand-side is

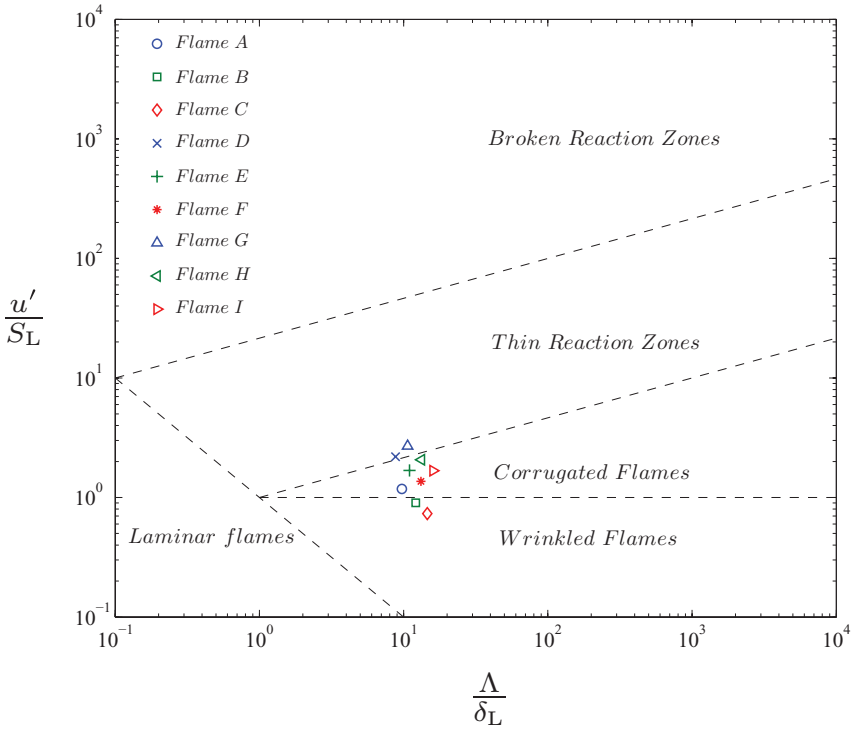

FIG. 3. Experimental conditions overlaid on the premixed combustion regime diagram.[1]

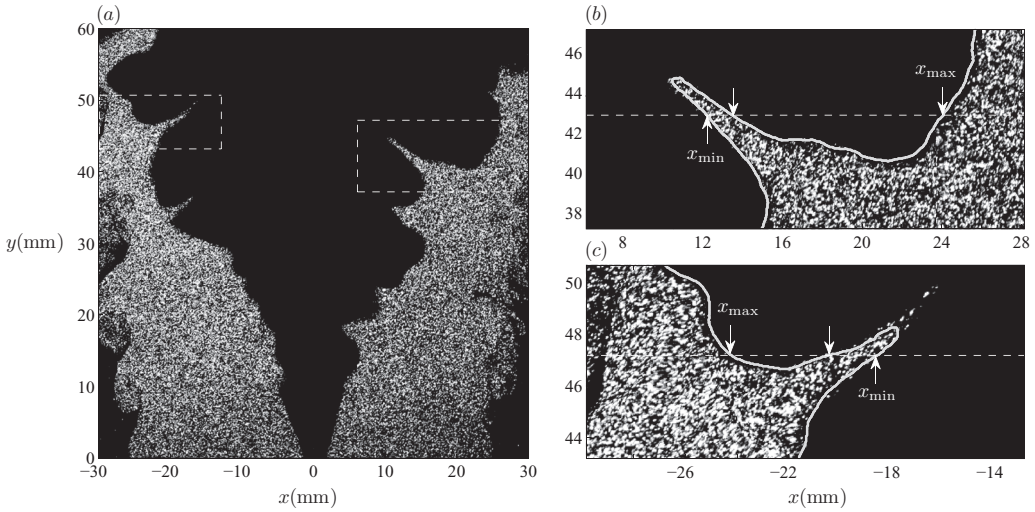

FIG. 4. Flame front position. (a) Representative Mie scattering image corresponding to Flame A condition and (b) and (c) insets of (a).

referred to as the left wing. Two insets of the Fig. 4(a) that correspond to the right and the left wings are presented in Figs. 4(b) and 4(c), respectively. The results in Figs. 4(b) and 4(c) depict that, at $y = 43$ mm and $y = 47$ mm, the flame front may have several positions. These positions are shown by arrows in the figures. For both right and left wings, x_{min} and x_{max} refer to flame front positions with minimum and maximum distances from the y-axis, respectively.

Arithmetic mean of x_{min} and x_{max} for both right and left wings of the flame front and for all experimental conditions are presented in Figs. 5(a)–5(c). In the figures, boundaries of each colorful area are associated with x_{min}/d and x_{max}/d of the corresponding experimental condition. For example, the inset of Fig. 5(a) shows that, for Flame A and at $y/d = 26$, $\overline{x_{min}}/d$ and $\overline{x_{max}}/d$ are 9 and 9.5, respectively. For all the experimental conditions tested and for both right and left wings, increasing the normalized vertical distance from the flame-holder (y/d) increases both $\overline{x_{min}}$ and $\overline{x_{max}}$ (Figs. 5(a)–5(c)). This is in agreement with the results presented by Lipatnikov and Chomiak.[5] At a fixed vertical distance from the flame-holder and for a given mean streamwise exit velocity, the results show that increasing the fuel-air equivalence ratio from 0.7 to 0.9 increases both $\overline{x_{min}}$ and $\overline{x_{max}}$.

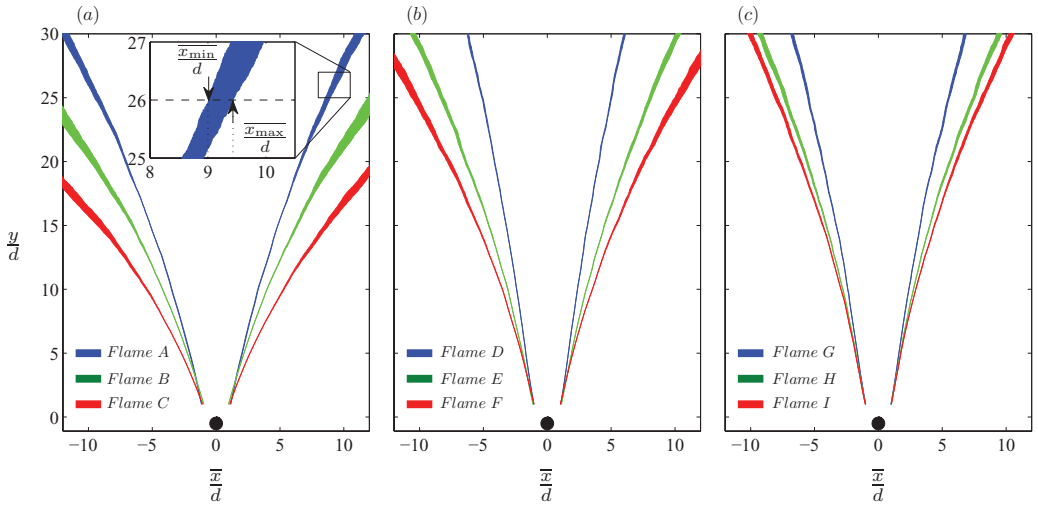

FIG. 5. Mean position of the flame front. (a), (b), and (c) correspond to $U = 4.0$, 6.2, and 8.6 m/s, respectively.

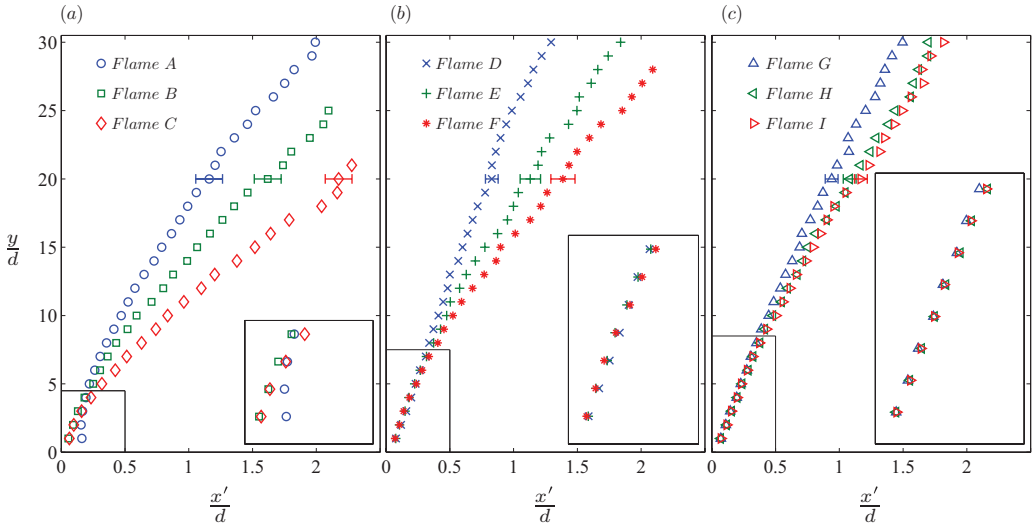

FIG. 6. Root-mean-square of flame front position. (a), (b), and (c) correspond to $U = 4.0$, 6.2, and 8.6 m/s, respectively.

The increase is more pronounced at large vertical distances from the flame-holder. For example, at mean streamwise exit velocity of $U = 4.0$ m/s and at $y/d = 5$, increasing ϕ from 0.7 to 0.9 increases $\overline{x_{\min}}/d$ by about 25%; whereas, at the same mean streamwise exit velocity and at $y/d = 15$, increasing ϕ from 0.7 to 0.9 increases $\overline{x_{\min}}/d$ by about 70%. At a fixed distance from the flame-holder and fixed fuel-air equivalence ratio, increasing the mean streamwise exit velocity decreases both $\overline{x_{\min}}/d$ and $\overline{x_{\max}}/d$. For example, comparison of the results associated with the experimental conditions of Flames A and G show that, at $y/d = 15$ and $\phi = 0.7$, increasing the mean streamwise exit velocity from 4.0 to 8.6 m/s decreases $\overline{x_{\min}}/d$ by approximately 50%.

The results presented in Fig. 5 show that the statistics of $x_{\min}$ is different from that of $x_{\max}$. For the results to be presented here, position of the flame front at a given vertical distance from the flame-holder is selected to be $x_{\min}$ corresponding to the right wing of the flame front, and is referred to as x. Variation of normalized RMS of x with normalized vertical distance from the flame-holder is presented in Figs. 6(a)–6(c). The estimated uncertainty associated with each experimental condition is presented by the error bars on the corresponding figure. For all the experimental conditions tested, increasing the distance from the flame-holder increases the RMS of the flame front position. Close to the flame-holder, x'/d is almost independent of ϕ and increases linearly with increasing y/d. The linear correlation between x'/d and y/d has been previously reported by Lipatnikov and Chomiak.[5] Least-square fits to the data presented in the insets of Figs. 6(a)–6(c) show that slopes of the fits are nearly constant and equal to 24. In comparison to the results presented for variation of x'/d with y/d for small vertical distances from the flame-holder, for relatively large vertical distances from the flame-holder, results presented in Figs. 6(a)–6(c) depict that x'/d significantly depends on the experimental condition tested. At a fixed mean streamwise exit velocity, increasing the fuel-air equivalence ratio from 0.7 to 0.9 increases x'/d. This increase is more pronounced at smaller values of mean streamwise exit velocity. For example, at $U = 4.0$ m/s and at $y/d = 15$, increasing the fuel-air equivalence ratio from 0.7 to 0.9 increases x'/d by about 100%; whereas, this increase is about 50% and 25% for $U = 6.2$ m/s and 8.6 m/s, respectively. The increase of x'/d with y/d at relatively large vertical distances from the flame-holder is in agreement with the results of Lipatnikov and Chomiak.[5] However, in comparison to the results of the present study that show x'/d significantly depends on ϕ, discussions presented by Lipatnikov and Chomiak[5] indicate that x'/d is independent of the fuel-air equivalence ratio.

The probability-density-function of the flame front position was estimated at several normalized vertical distances from the flame-holder. A representative PDF of the flame front position corresponding to Flame A condition is shown in Fig. 7(a). Estimated values of the PDF at $y/d = 5$, 15, and 25 are presented in Fig. 7(b). The PDFs feature a bell-shaped distribution. Indeed, this was observed

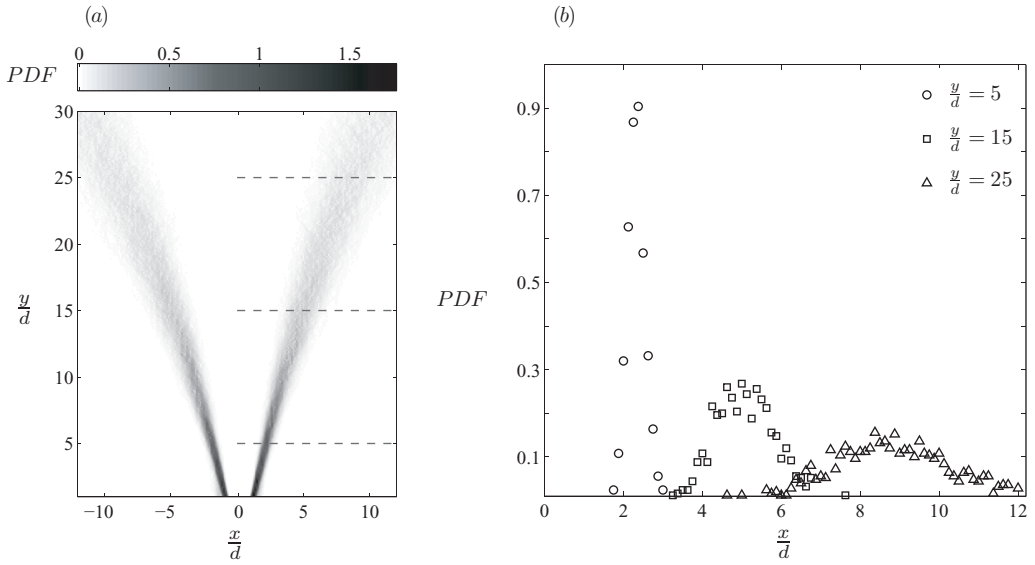

FIG. 7. (a) Contour of probability-density-function and (b) representative probability-density-functions estimated at $y/d = 5$, 15, and 25. The results in both (a) and (b) correspond to experimental condition of Flame A.

for all the experimental conditions tested and is in agreement with the results previously reported by Shepherd *et al.*[6] and Namazian *et al.*[7] These studies[6,7] suggest that, at a given vertical distance from the flame-holder, the PDF of the flame front position can be represented by a Gaussian distribution, or mathematically: $PDF(x) = \frac{1}{x'\sqrt{2\pi}} e^{-\frac{1}{2}(\frac{x-\overline{x}}{x'})^2}$. Introducing $PDF^*(x) = PDF(x)/\max(PDF(x))$, it can be shown that

$$\ln(-\ln(PDF^*)) = 2\ln(|\frac{x-\overline{x}}{x'}|) - 0.7. \quad (1)$$

Estimated values of $\ln(-\ln(PDF^*))$ and $\ln(|\frac{x^- - \overline{x}}{x'}|)$, where x^- represents $x < \overline{x}$ are shown in Fig. 8(a). The results in the figure are associated with flame front position measured at $y/d = 15$. As shown in Fig. 8(a), for relatively large values of $\ln(|\frac{x^- - \overline{x}}{x'}|)$, the data follow a linear trend. The extent of the region over which the data in Fig. 8(a) represent a linear variation was obtained using the following rationale.

As an initial guess, the region associated with $\ln(|\frac{x^- - \overline{x}}{x'}|) > 0.5$, i.e., $x^- \lesssim \overline{x} - 1.6x'$, was utilized as the range over which the PDF data show a linear trend. Then, a line was fit to the data pertaining to $x^- \lesssim \overline{x} - 1.6x'$. Two bounds, each with vertical extent equal to the uncertainty of the PDF data, were considered at the top and the bottom of the line fit. Using the uncertainty bounds along with an iterative technique, extent of the region $x^- \lesssim \overline{x} - 1.6x'$ was modified to $x^- \lesssim \overline{x} - 1.3x'$. Conducting a sensitivity analysis, it was obtained that the range associated with the linear variation of the PDF data, i.e., $x^- \lesssim \overline{x} - 1.3x'$, is independent of the initial guess, i.e., $\ln(|\frac{x^- - \overline{x}}{x'}|) > 0.5$.

The region associated with the linear variation in the PDF data is enlarged and presented in Fig. 8(b). The gray colored region in the figure corresponds to the uncertainty bound of the PDF data. The least-square technique was used to fit a line to the data in the region: $x^- \lesssim \overline{x} - 1.3x'$. The mathematical interpretation of the line is identical to that presented in Eq. (1). Thus, it can be concluded that for the results presented in Fig. 8(b), i.e., $x^- \lesssim \overline{x} - 1.3x'$, PDF of the flame front position has a Gaussian distribution. In comparison to the results presented for $\ln(|\frac{x^- - \overline{x}}{x'}|) \gtrsim 0.3$, the data presented in Fig. 8(a) associated with $\ln(|\frac{x^- - \overline{x}}{x'}|) \lesssim 0.3$ are scattered and do not follow the trend predicted by Eq. (1). Thus, for $\ln(|\frac{x^- - \overline{x}}{x'}|) \lesssim 0.3$, i.e., $\overline{x} - 1.3x' < x^- \lesssim \overline{x}$, the PDF of the flame front position does not have a Gaussian distribution.

The technique presented here for studying the characteristics of the PDF results, i.e., transformation of the PDF data to the logarithmic domain and then obtaining the line fit to the data,

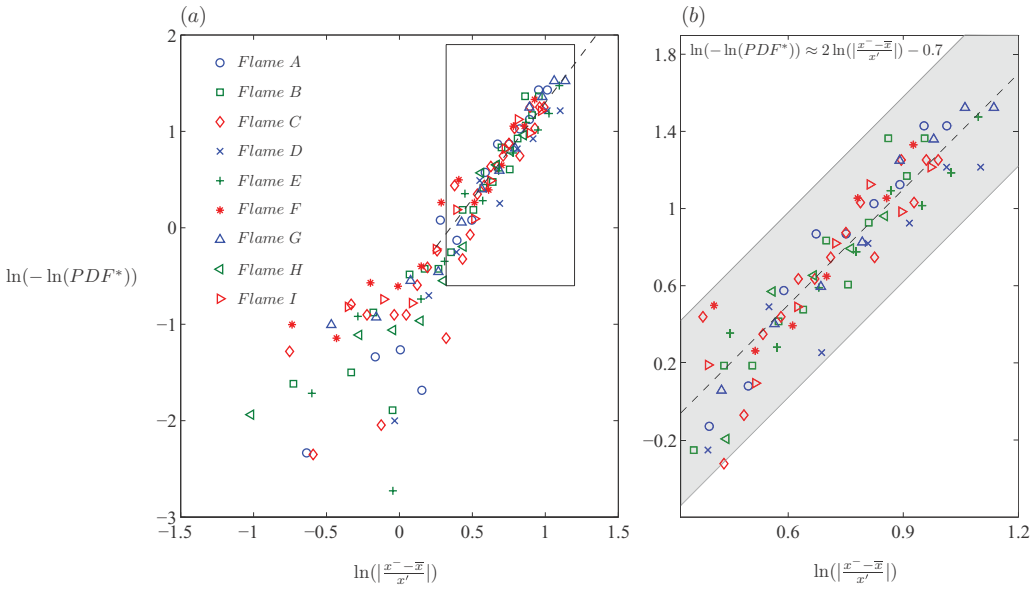

FIG. 8. (a) Probability-density-function of flame front position at $y/d = 15$ and for $x < \overline{x}$ and (b) the inset of (a).

allows for quantifying the extent of the region over which the data have a bell-shaped distribution. This technique was also utilized for studying probability-density-functions of other characteristics of flame front, e.g., PDF of flame front curvature.

Variation of $\ln(-\ln(PDF^*))$ with $\ln(|\frac{x^+ - \overline{x}}{x'}|)$, where x^+ represents $x > \overline{x}$, is shown in Fig. 9(a). Using the technique presented for analyzing PDFs of x^-, it was obtained that, for $\ln(|\frac{x^+ - \overline{x}}{x'}|) \gtrsim 0.2$, i.e., $x^+ \gtrsim \overline{x} + 1.2x'$, the data collapse onto a line. The region over which $\ln(-\ln(PDF^*))$ has a linear relationship with $\ln(|\frac{x^+ - \overline{x}}{x'}|)$ is presented in Fig. 9(b). Using a least-square technique, the fit

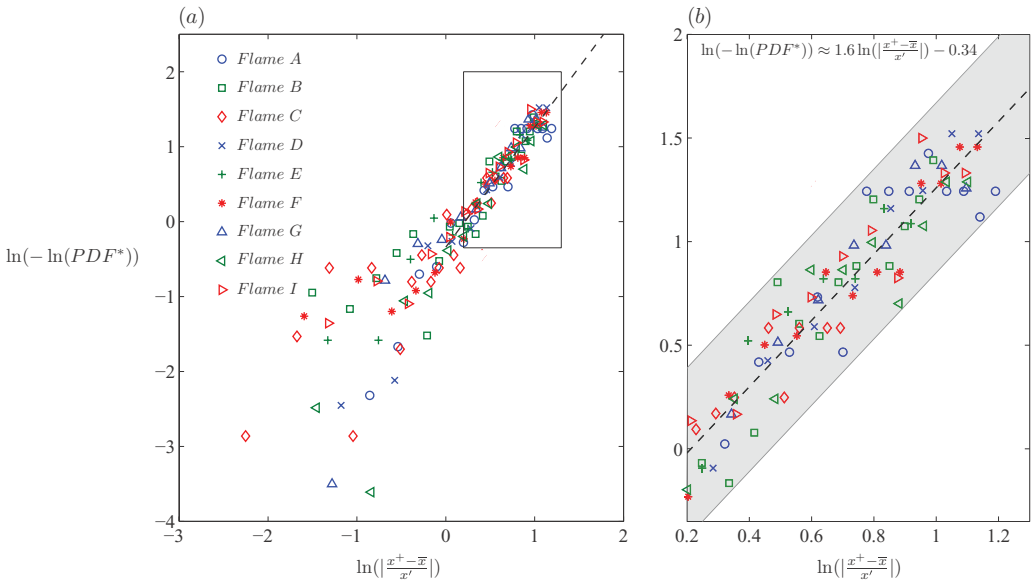

FIG. 9. (a) Probability-density-function of flame front position at $y/d = 15$ and for $x > \overline{x}$ and (b) the inset of (a).

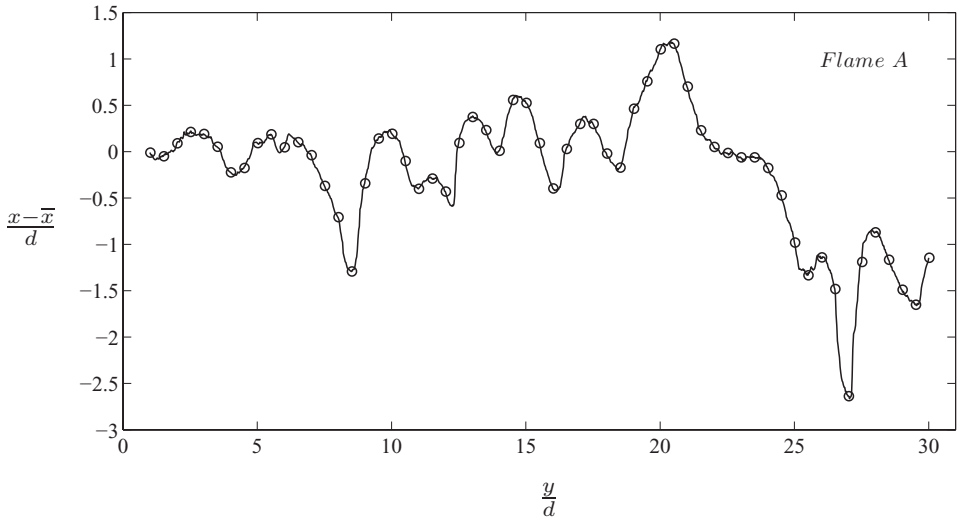

FIG. 10. Representative signal of flame front oscillations utilized for FFT calculations. The hollow symbol corresponds to the data sampled at a resolution of 1 mm. The results pertain to Flame A condition.

to the data in Fig. 9(b) was obtained and presented in Eq. (2).

$$\ln\left(-\ln\left(PDF^*\right)\right) = 1.6\ln\left(\left|\frac{x^+ - \overline{x}}{x'}\right|\right) - 0.34. \tag{2}$$

The equation is different from that obtained for a Gaussian distribution, i.e., Eq. (1). Thus, for $x^+ \gtrsim \overline{x} + 1.2x'$, although the PDF of the flame front position shows a bell-shaped distribution, the distribution is not Gaussian. The gray region in Fig. 9(b) represents the uncertainty bounds associated with the PDF data. For $\ln\left|\left(\frac{x^+-\overline{x}}{x'}\right)\right| \lesssim 0.2$, i.e., $\overline{x} < x^+ < \overline{x} + 1.2x'$, the results shown in Fig. 9(a) are scattered and do not lie on the line presented by Eq. (2).

Results presented in Fig. 4 depicted that the flame fronts investigated in the present study can be significantly wrinkled. Using the Fast-Fourier-Transform (FFT) technique, spectral analysis was performed to investigate relative energy of the wave numbers that contribute to wrinkling of the flame front. The fluctuations of the flame front position, i.e., $x - \overline{x}$, along the y-axis was utilized for the FFT analysis. The solid curve presented in Fig. 10 shows a representative variation of $x - \overline{x}$ with y corresponding to Flame A condition. For the FFT analysis, the resolution of the flame front position data (Δy), i.e., vertical distance between two neighboring points, was selected to be 1 mm. This resolution corresponds to the maximum inner cutoff scale of all of the experimental conditions tested. The hollow circles shown in Fig. 10 represent the data points pertaining to the solid curve sampled at a resolution of 1 mm. The number of data points utilized for the FFT analysis (n) is the largest integer number, which is smaller than or equal to $n = (y_{\max} - y_{\min})/\Delta y + 1$. $y_{\min}$ and $y_{\max}$ are the minimum and the maximum vertical distances between the flame front and the flame-holder, respectively. For all experimental conditions tested, the minimum vertical distance from the flame-holder was selected to be 2 mm. The maximum vertical distance, $y_{\max}$, depends on the experimental condition tested. For example, for the results presented in Fig. 10, $y_{\max}$ is 60 mm and, as a result, $n = 59$. In order to avoid noise in FFT calculation, the number of points used for FFT operation (n_{FFT}) has to be smaller than the number of points used to represent the flame front position data, or $n_{\mathrm{FFT}} < n$. For all the experimental conditions tested, 32 points ($n_{\mathrm{FFT}} = 2^5$) were used for power-spectrum-density (PSD) calculations.

Note that, since the flame front position signal develops with vertical distance from the flame-holder (see Fig. 10), the PSDs are dependent on the length of the signal utilized for the analyses. Specifically, sensitivity tests show that the PSD values change by varying $y_{\min}$ and $y_{\max}$. For the results presented in this study, $y_{\min}$ and $y_{\max}$ were selected in order to maximize the length of the flame front position signal.

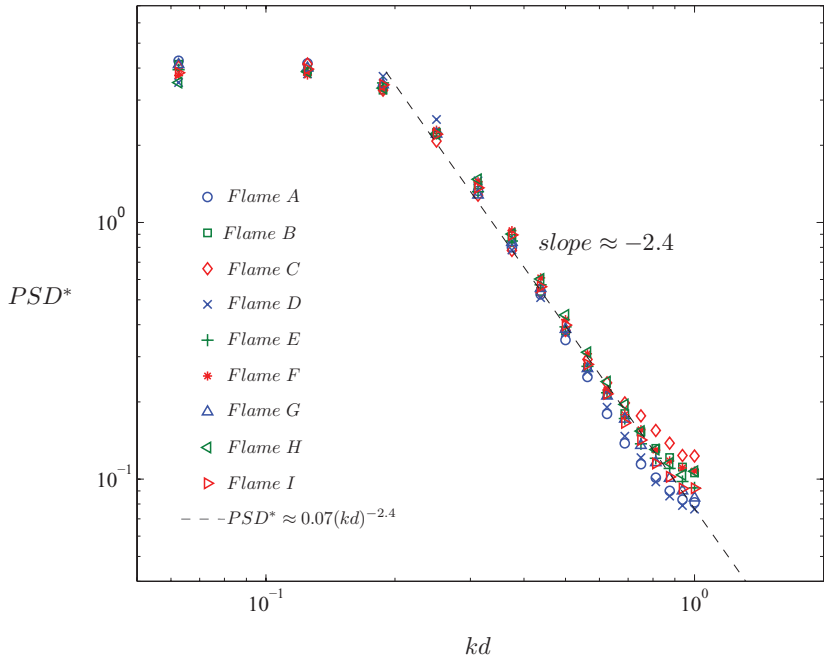

FIG. 11. Power-spectrum-density of flame front position.

The results presented in Fig. 10 show that the signal of $x - \overline{x}$ is not periodic. This non-periodicity can cause spectral leakage in PSD calculation.[31] In order to avoid this, the Hanning window function was applied to the PSD calculation. Analysis of the results shows that the PSDs are not sensitive to the choice of the window function.

For each experimental condition, the calculated PSDs were averaged for all recorded images. The averaged PSDs were normalized by the area under the curve of averaged PSD against the wave number (k). The estimated normalized and averaged power-spectrum-density (PSD^*) along with the normalized wave number (kd) is presented in Fig. 11. In the figure, the maximum value of the normalized wave number is equal to ratio of flame-holder diameter to twice the resolution of the flame front position data, i.e., $d/(2\Delta y) = 1$. The minimum value of the normalized wave number is equal to ratio of flame-holder diameter to the resolution of flame front position data times the number of points used in FFT calculations, i.e., $d/(n_{\mathrm{FFT}}\Delta y) = 1/16$. The values of the normalized and averaged power-spectrum-densities are almost independent of the experimental conditions tested, as shown in Fig. 11. Specifically, for $kd \lesssim 0.2$, PSD^* is almost constant and equals to four. However, for $kd \gtrsim 0.2$, the results show a linear trend. The least-square technique was utilized to fit a line to the data presented in Fig. 11 for $0.2 \lesssim kd < 1$. Since the results in Fig. 11 are presented in a logarithmic scale, the linear trend observed for $0.2 \lesssim kd < 1$ is equivalent to a power-law correlation between the PSD^* and the normalized wave number. Mathematical interpretation of the correlation is provided below.

$$PSD^* \approx 0.07(kd)^{-2.4}. \tag{3}$$

The wave number (k) presented in Fig. 11 was normalized by the flame-holder diameter. In order to facilitate a comparison between the results of different experimental test rigs, the wave number data can be normalized by a length scale associated with the size of flame front wrinkling. Atashkari *et al.*[14] proposed the flame front wrinkling scale (L) to estimate a characteristic length scale for flame front wrinkling. The flame front wrinkling scale is given by the following equation:

$$L = \int_0^{y_0} R_{xx}\mathrm{d}y, \tag{4}$$

TABLE III. Length scales associated with flame front characteristics. U, ϕ, Λ, L, and κ' are the mean streamwise exit velocity, fuel-air equivalence ratio, integral length scale, flame front wrinkling scale, and the RMS of the curvature data, respectively. The uncertainty associated with estimation of both Λ and L is 0.4 mm. k_c and k_θ are the wave numbers at which the power-spectrum-densities of κ and θ feature a peak, respectively.

	Symbol	U(m/s)	ϕ	Λ(mm)	L(mm)	$1/\kappa'$(mm)	$1/k_c$(mm)	$1/k_\theta$(mm)
Flame A	○	4.0	0.7	2.1	1.9	3 ± 1	16 ± 4	16 ± 4
Flame B	□	4.0	0.8	2.1	2.6	2 ± 1	11 ± 2	16 ± 4
Flame C	◇	4.0	0.9	2.1	2.4	2 ± 1	11 ± 2	13 ± 3
Flame D	×	6.2	0.7	1.9	2.4	2 ± 1.5	9 ± 1	16 ± 4
Flame E	+	6.2	0.8	1.9	2.5	2 ± 1.5	7 ± 1	13 ± 3
Flame F	*	6.2	0.9	1.9	2.5	2 ± 1	7 ± 1	13 ± 3
Flame G	△	8.6	0.7	2.3	2.5	2 ± 1.5	8 ± 1	13 ± 3
Flame H	◁	8.6	0.8	2.3	2.6	2 ± 1	9 ± 1	13 ± 3
Flame I	▷	8.6	0.9	2.3	2.8	1.5 ± 1	7 ± 1	13 ± 3

where R_{xx} is the autocorrelation of position of the flame front. In Eq. (4), y_0 is the location where the autocorrelation function first crosses the y-axis. The values of flame wrinkling scale are presented in Table III. Also included in Table III are the values of the integral length scale. The uncertainty associated with calculation of both flame front wrinkling scale and the integral length scale was ± 0.4 mm. Comparison of the flame wrinkling scale data, L, with the integral length scale, Λ, shows that, for all the tested conditions, the values of L are similar to those of Λ. This implies that the large eddies in the incident turbulent flow play a significant role in the wrinkling process of turbulent flames investigated in the present study. Table III includes other length scales associated with the flame front which will be discussed in Secs. III C and III D.

The horizontal axis in Fig. 11 was normalized by the flame wrinkling scale (kL) and was presented in Fig. 12. The results by Atashkari *et al.*[14] are also provided in the figure. Study of Atashkari *et al.*[14] was performed on three different flame configurations: V-shaped flame, spherical flame, and flames in a reciprocating engine. Their results[14] are presented by solid symbols and the results corresponding to the present study are shown by hollow symbols. Comparison of the results associated with Flames A-I indicate that the PSD^* values associated with Flame A are smaller than

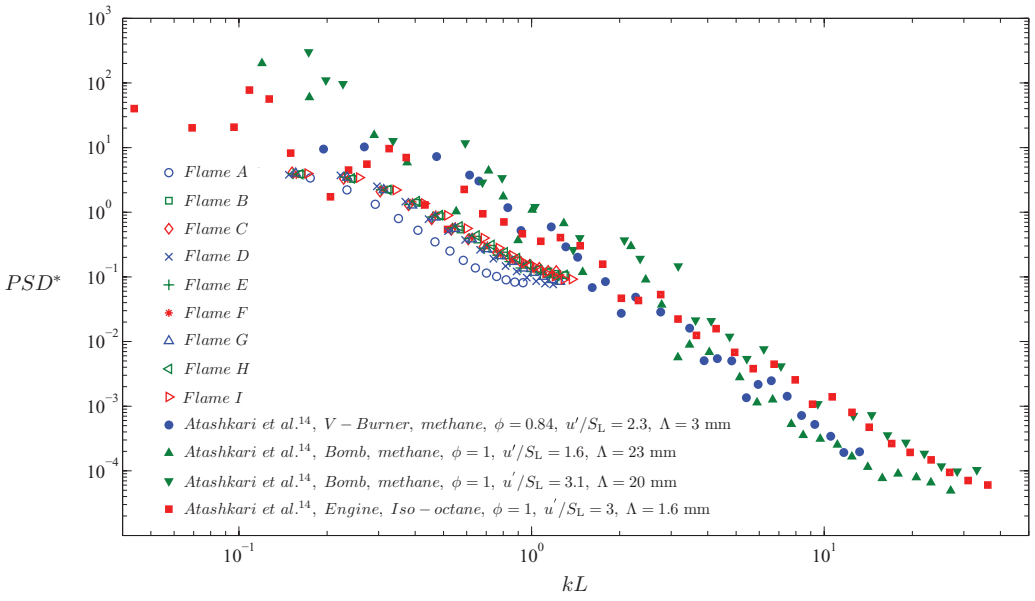

FIG. 12. Power-spectrum-densities associated with the present study and those associated with Atashkari *et al.*[14]

those pertaining to the rest of the experimental conditions tested. This is linked to small value of the flame front wrinkling scale utilized for normalization of Flame A data in comparison to those used for normalization of data associated with Flames B-I. Comparison of the results of the present study and those of Atashkari *et al.*[14] shows that the trend of variation of *PSD** with *kL* in both investigations are similar. This similarity suggests that the decaying trend of normalized power-spectrum-density with the normalized wave number is universal and independent of the flame geometries investigated. However, comparison of the *PSD** values presented in Atashkari *et al.*[14] with those of the present study indicates that the values of the normalized power-spectrum-densities do not collapse. This discrepancy is expected to be associated with the following reasons.

First, the maximum normalized wave number utilized for the study of Atashkari *et al.*[14] is larger than that used for the present study. Specifically, the normalized wave number corresponding to the study of Atashkari *et al.*[14] is more than approximately 10; whereas, this parameter is about unity for the present study. It was previously shown that the maximum wave number is inversely correlated with the resolution of the flame front contour. Comparison of the resolutions utilized for the present study and for the study of Atashkari *et al.*[14] shows that the resolution used in Atashkari *et al.*[14] is more than 3 times smaller than that of the present study. Thus, the maximum wave number used in Atashkari *et al.*[14] is expected to be larger than that of the present study. The second reason is linked to the different flame geometries investigated in both studies. Discussions presented by Driscoll[4] show that the characteristics of turbulent premixed flames are highly influenced by the flame front geometries. Thus, the differences between the values of *PSD** measured in Atashkari *et al.*[14] and those in the present study are expected to be partly associated with the different flame front geometries investigated in the corresponding studies.

B. Flame brush thickness

The flame brush thickness (δ_t) was calculated using the mean-progress-variable ($\overline{c}$). The mean-progress-variable was estimated from averaging the binarized images obtained from the Mie scattering technique. A representative contour of $\overline{c}$ estimated for experimental condition corresponding to Flame A is shown in Fig. 13(a). The results presented in the figure are similar to those presented in previous studies, see, for example, Bell *et al.*,[16] Knaus and Gouldin,[18] and Shepherd.[32] Variation

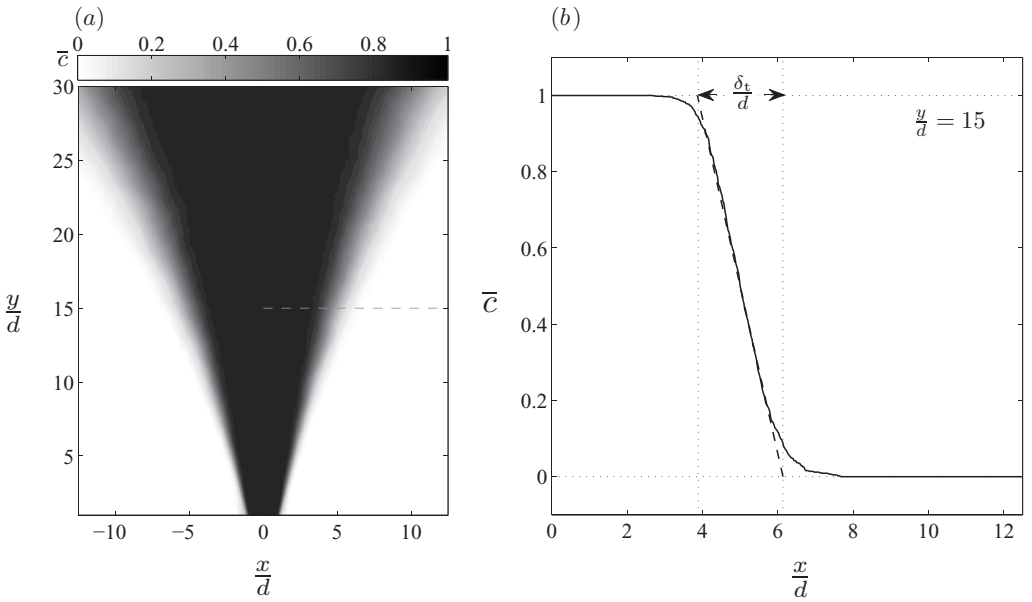

FIG. 13. Mean-progress-variable corresponding to experimental condition of Flame A. (a) Contour of $\overline{c}$ and (b) representative variation of $\overline{c}$ with x/d at $y/d = 15$.

of the mean-progress-variable across the flame region and at $y/d = 15$ is provided in Fig. 13(b). The variation is similar to a complementary error function. For such a distribution of the mean-progress-variable, it can be mathematically shown that $\mathrm{d}\overline{c}/\mathrm{d}x$ has a Gaussian distribution given by the following equation:

$$\frac{\mathrm{d}\overline{c}}{\mathrm{d}x} = \frac{-1}{x'\sqrt{2\pi}} e^{-\frac{1}{2}\left(\frac{x-\overline{x}}{x'}\right)^2}. \tag{5}$$

As proposed by Namazian *et al.*,[7] the flame brush thickness is the ratio of the density change across the flame region to the maximum of the mean density gradient, i.e., $\delta_t = (\rho_u - \rho_b)/\max(\mathrm{d}\overline{\rho}/\mathrm{d}x)$. Using the mean-progress-variable definition, i.e., $\overline{c} = (\overline{\rho} - \rho_u)/(\rho_b - \rho_u)$, the formulation proposed by Namazian *et al.*[7] can be simplified to

$$\delta_t = \frac{1}{\max(-\mathrm{d}\overline{c}/\mathrm{d}x)}. \tag{6}$$

Assuming $-\mathrm{d}\overline{c}/\mathrm{d}x$ maximizes at $x = \overline{x}$, which is mathematically in agreement with Eq. (5), the formulation proposed by Namazian *et al.*[7] can be further simplified into $\delta_t = 1/(-\mathrm{d}\overline{c}/\mathrm{d}x)|_{x=\overline{x}}$. Combining the simplified equation of the flame brush thickness and Eq. (5), the following formulation is obtained for the flame brush thickness.

$$\delta_t = \sqrt{2\pi}x'. \tag{7}$$

Equation (7) indicates that the flame brush thickness has a linear relationship with RMS of the flame front position, with a slope of $\sqrt{2\pi} \approx 2.51$.

In the present study, Eq. (6) was utilized to estimate the flame brush thickness. Correlation between the flame brush thickness and the RMS of the flame front position is shown in Fig. 14. The results are presented for several vertical distances from the flame-holder and for all experimental conditions tested. Representative error bars associated with estimations of the uncertainties pertaining to RMS flame front position and flame brush thickness are provided in the figure. In agreement with the results presented in Eq. (6), δ_t has a linear relationship with x'. The least-square technique was utilized to fit a line to the data presented in Fig. 14. The slope of the line obtained from the

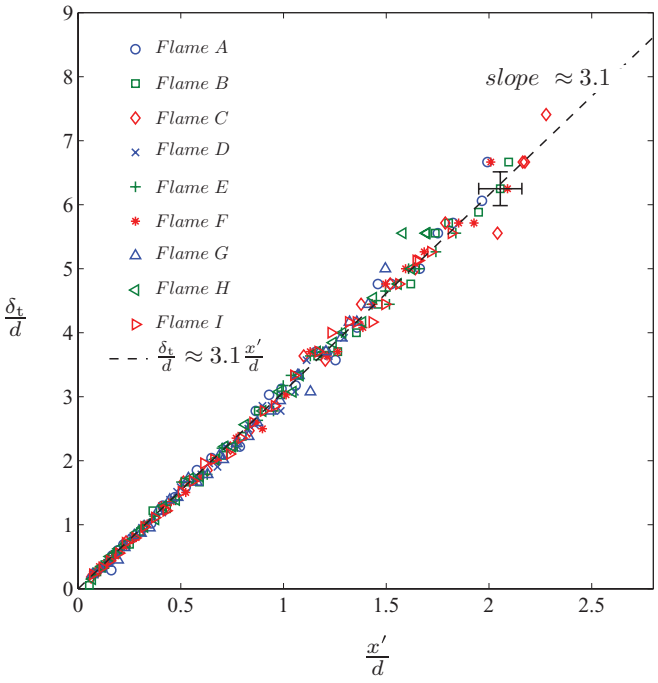

FIG. 14. Variation of the flame brush thickness with the RMS of flame front position.

experimental results is 3.1. This slope differs by approximately 20% from that of the line presented in Eq. (6). A rationale for this discrepancy is provided below.

For the experimental conditions associated with the flamelet regime, the PDF of the flame front position is directly correlated with $d\overline{c}/dx$. It was previously shown that the PDF of the flame front position is not Gaussian for $x > \overline{x}$ (see Fig. 9). Thus, $d\overline{c}/dx$ is not expected to feature a Gaussian distribution for $x > \overline{x}$. As a result, the mathematical formulation provided in Eq. (5) may not accurately model $d\overline{c}/dx$. Thus, it is expected that the slope of the line estimated from the mathematical formulation would be different from that obtained from the experiments.

C. Flame front curvature

The flame front curvature (κ) was estimated along the right wing of the flame front using the following equation:

$$\kappa = \frac{\dot{y}\ddot{x} - \dot{x}\ddot{y}}{(\dot{x}^2 + \dot{y}^2)^{\frac{3}{2}}}, \tag{8}$$

where x and y correspond to the horizontal and vertical positions of the flame front, respectively. The symbol $(\cdot)$ represents derivative with respect to length of the flame front. Using the three-point finite differencing scheme,[33] Eq. (8) can be discretized into the following equation:

$$\kappa_i = \frac{8[x_{i-1}(y_{i+1} - y_i) + x_i(y_{i-1} - y_{i+1}) + x_{i+1}(y_i - y_{i-1})]}{[(x_{i+1} - x_{i-1})^2 + (y_{i+1} - y_{i-1})^2]^{\frac{3}{2}}}, \tag{9}$$

where the index i corresponds to the ith point along the flame front. In Eq. (9), the neighboring points along the flame front were selected such that the distance between them was equal to the inner cutoff scale of the corresponding experimental condition.[26]

For all the experimental conditions tested, the mean value of the curvature of the flame front ($\overline{\kappa}$) was zero. The uncertainty associated with estimation of $\overline{\kappa}$ was ± 0.4 mm^{-1}. The zero value of the mean curvature data is in agreement with previous experimental results associated with bluff-body stabilized and Bunsen type flames, see, for example, Soika *et al.*[34] and Yuen and Gülder.[35] Root-mean-square of the curvature data (κ') was estimated, and $1/\kappa'$ was tabulated in Table III. The uncertainties in estimation of $1/\kappa'$ are also presented. As shown in the table, values of $1/\kappa'$ are almost insensitive to variation in the experimental conditions tested. Comparison of the results presented in the table shows that values of $1/\kappa'$ are similar to those of the integral length scale and the flame front wrinkling scale. This means that the large scale turbulent structures in the flow significantly affect the wrinkling of the flame front.

For each experimental condition tested, PDF of the flame front curvature was estimated along the right wing of the flame front and for all acquired images. A representative PDF of the flame front curvature data, corresponding to Flame A, is presented in Fig. 15. As shown in the figure, the flame front curvature has a bell-shaped distribution. This is similar to those associated with other flame geometries, such as those pertaining to bluff-body stabilized[34] and Bunsen type flames.[35] Results presented in these studies indicate that the PDF of the flame front curvature is symmetric. In order to investigate the symmetry of the PDF data with respect to $\kappa = 0$, the results were transferred to a logarithmic scale, similar to that presented in Figs. 8 and 9.

Estimated values of $\ln(-\ln(PDF^*))$ and $\ln(|\frac{\kappa^-}{\kappa^{-'}}|)$, where κ^- represents negative values of curvature data and $\kappa^{-'}$ is the RMS of the negative curvature data, are presented in Fig. 16. The negative curvature corresponds to the flame front concave to the unburnt gas and positive curvature corresponds to the flame front convex to the unburnt gas.[9,10,36] Two regions can be identified in Fig. 16(a). For the first region, $\ln(-\ln(PDF^*))$ shows a linear relationship with $\ln(|\frac{\kappa^-}{\kappa^{-'}}|)$. Extent of the region over which the linear relationship is valid was obtained using the technique previously presented for analyzing PDF of the flame front position data (Figs. 8 and 9). Analysis of the data shows that $\ln(-\ln(PDF^*))$ is linearly correlated with $\ln(|\frac{\kappa^-}{\kappa^{-'}}|)$ for $\ln(|\frac{\kappa^-}{\kappa^{-'}}|) \gtrsim 1$, or $\kappa^- \lesssim -2.7\kappa^{-'}$. This region is shown in Fig. 16(b). The least-square technique was used to fit a line to the data in

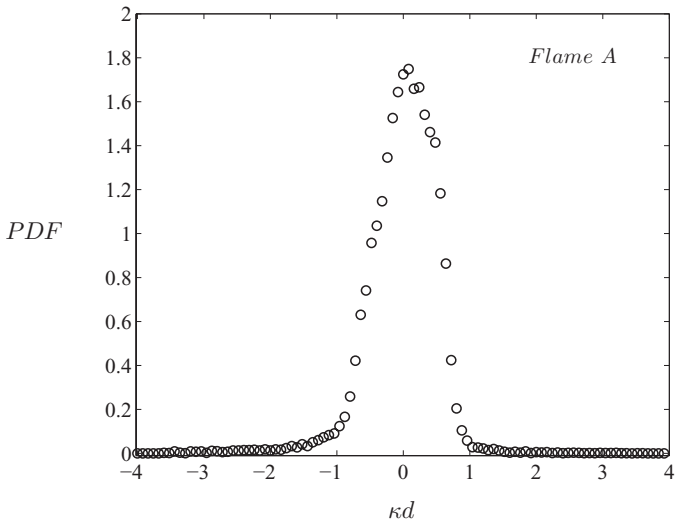

FIG. 15. Probability-density-function of the flame front curvature data corresponding to Flame A.

Fig. 16(b). Equation of the line is given by

$$\ln(-\ln(PDF^*) = 0.74\ln(|\frac{\kappa^-}{\kappa^{-'}}|) + 0.4. \tag{10}$$

The vertical extent of the gray area shown in Fig. 16(b) pertains to twice the uncertainty associated with estimating the PDF of the curvature data. Equation (10) indicates that the PDF of the curvature data is not Gaussian for $\kappa^- < -2.7\kappa'$. The second region in Fig. 16(a) corresponds to $-2.7\kappa^{-'} \lesssim \kappa^- < 0$. In this region, the PDF^* values are significantly dependent on the experimental conditions tested and show scatter.

The normalized PDF of the positive curvature data are presented in Fig. 17. In the figure, κ^+ represents the positive values of curvature, and $\kappa^{+'}$ is the RMS of κ^+. Three regions can be identified in Fig. 17(a). The first and second regions correspond to the $\ln(|\frac{\kappa^+}{\kappa^{+'}}|) \gtrsim 1.4$ (or $\kappa^+ \gtrsim 4.1\kappa^{+'}$) and $0.1 \lesssim \ln(|\frac{\kappa^+}{\kappa^{+'}}|) \lesssim 1.4$ (or $1.1\kappa^{+'} \lesssim \kappa^+ \lesssim 4.1\kappa^{+'}$), respectively. Extents of these regions were obtained using the methodology previously utilized for the analyses of the PDFs presented in

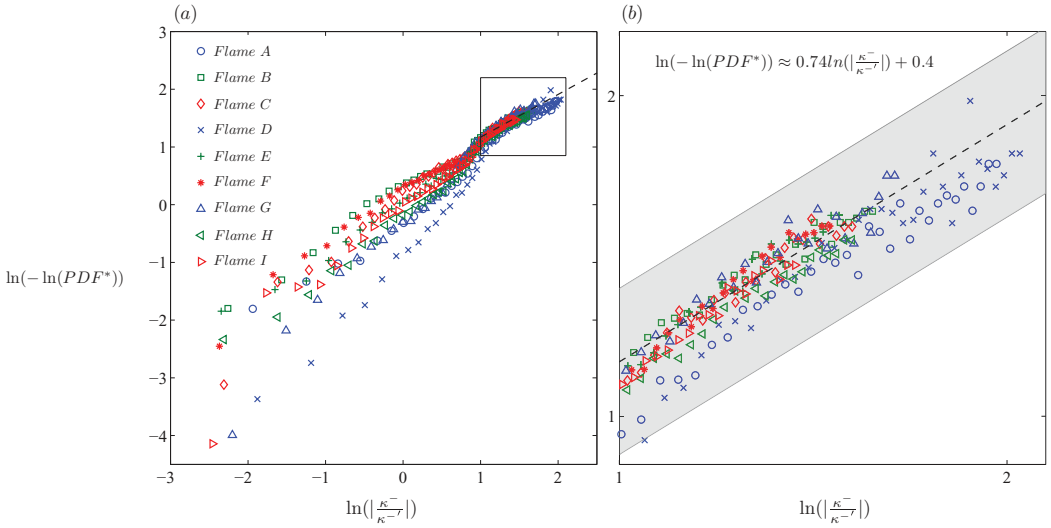

FIG. 16. (a) Probability-density-function of negative values of the curvature and (b) the inset of (a).

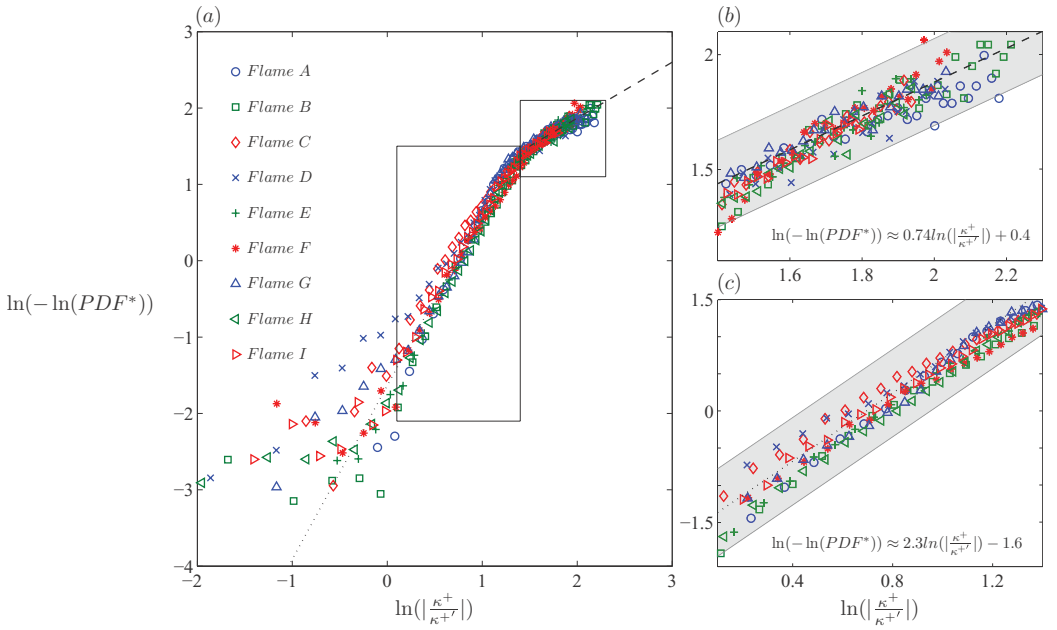

FIG. 17. (a) Probability-density-function of positive values of the curvature data. (b) and (c) are the insets of (a).

Figs. 8, 9, and 16. The first and second regions are enlarged and presented in Figs. 17(b) and 17(c), respectively. The least-square technique shows that the fit to the data in Fig. 17(b) is identical to that previously obtained for $-2.7\kappa^{-'} \lesssim \kappa^- < 0$, with the results presented in Fig. 16(b). However, the least-square fit to the data in Fig. 17(c) shows that

$$\ln\left(-\ln\left(PDF^*(\kappa^+)\right)\right) = 2.3\ln\left(|\frac{\kappa^+}{\kappa^{+'}}|\right) - 1.6. \tag{11}$$

In Eq. (11), the slope of the line is larger than that obtained for the first region. This means that, for positive values of curvature of the flame front, the decay of the PDF of the curvature data for $1.1\kappa^{+'} \lesssim \kappa^+ \lesssim 4.1\kappa^{+'}$ is faster than the region associated with $\kappa^+ \gtrsim 4.1\kappa^{+'}$. The third region in Fig. 17(b) corresponds to $\ln(|\frac{\kappa^+}{\kappa^{+'}}|) \lesssim 0.1$, or $0 < \kappa^+ \lesssim 1.1\kappa^{+'}$. In comparison to the results presented for $\kappa^+ \gtrsim 1.1\kappa^{+'}$, which showed that the PDFs are independent of the experimental conditions tested, the results associated with $\kappa^+ \lesssim 1.1\kappa^{+'}$ illustrate that the PDF data significantly depend on the experimental conditions tested and show a scatter.

The Lewis number associated with the flame conditions investigated in the present study is close to unity, and, as a result, the effects of strain and curvature on the flame front are expected to be negligible. This means that the probabilities of formations of both negative and positive flame front curvatures should be similar, since the flame front behaves as a passive surface. Hence, the PDF of the flame front curvature is expected to be symmetric with respect to $\kappa = 0$. However, the results presented in Figs. 16 and 17 indicate that the flame front curvature is asymmetric with respect to $\kappa = 0$. The reason for this discrepancy is beyond the scope of this article and requires further investigations.

Power-spectrum-density of the curvature data along the right wing of the flame front was estimated using the Fast-Fourier-Transform technique. The resolution of the curvature data along the flame front (Δl) was selected to be 1 mm. This corresponds to the maximum inner cutoff scale of all the experimental conditions tested. The number of points selected along the flame front (n') is the integer number closest to and smaller than $n' = l/\Delta l$, where l is the length of the right wing of the flame front. For all the experimental conditions tested, at least 70 points were selected along the flame front. In order to avoid noise in calculation of FFT of the curvature data, the number of points used in FFT operation (n_{FFT}) was selected to be 64, or $n_{\mathrm{FFT}} = 2^6$. For each experimental

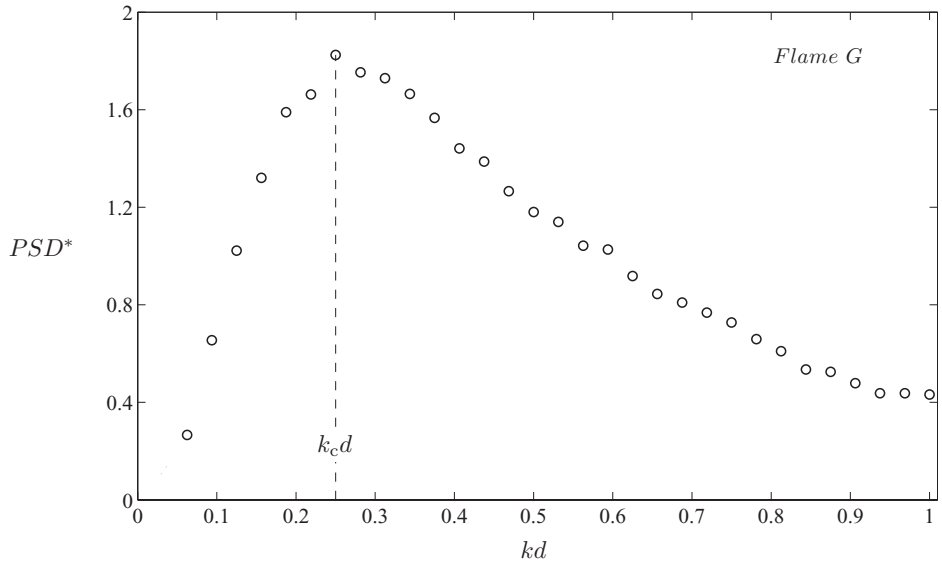

FIG. 18. Power-spectrum-density of curvature data estimated for experimental condition pertaining to Flame G.

condition tested, the power-spectrum-density was obtained from the FFT of the curvature data. In order to avoid leakage in FFT calculations, the Hanning window function was utilized for the PSD calculations. Analysis of the results shows that the PSDs are not sensitive to the choice of the window function. The averaged PSDs were normalized by area under the curve of averaged PSD against the wave number (k). A representative normalized and averaged power-spectrum-density (PSD^*) of the curvature data corresponding to experimental condition of Flame G is presented in Fig. 18. As shown in the figure, PSD^* features a peak at a normalized wave number of about 0.25. This means that, for the experimental condition corresponding to Flame G, the wave number of $k = 0.125$ makes the most contribution in energy of the curvature data. Examination of the PSD^* obtained for all the experimental conditions shows that, indeed, all the PSD^* distributions feature a peak. The wave number at which the peak occurs is referred to as k_c. The values of the inverse of this wave number ($1/k_c$) along with their pertaining uncertainties are tabulated in Table III. The results presented in the table show that values of $1/k_c$ are larger than the integral length scale, flame wrinkling scale, and the inverse of the RMS of curvature data. Comparisons of the values of $1/k_c$ at different burner exit velocities as well as different fuel-air equivalence ratios do not show a trend.

D. Flame front orientation

The orientation of the flame front is of significant importance in V-shaped flames since it can be utilized for estimating the flame surface density and the turbulent burning velocity, see, for example, Sattler *et al.*[19] The flame front orientation can be obtained either in the coordinate system with axes locally normal and tangent to the mean flame front location, or in the laboratory coordinate system, i.e., the Cartesian coordinate system presented in Figs. 1(b) and 2(b). In the present study, the flame front orientation was estimated in the Cartesian coordinate system. Specifically, the flame front orientation was studied using the angle between tangent to the flame front and the x-axis. This angle is referred to as θ and is given by the following equation:

$$\theta = \arctan\left(\frac{\dot{y}}{\dot{x}}\right), \tag{12}$$

where $(\dot{\cdot})$ represents derivative with respect to the length of the flame front. Using a forward differencing scheme,[33] Eq. (12) was discretized into the following equation:

$$\theta_i = \arctan\left(\frac{y_{i+1} - y_i}{x_{i+1} - x_i}\right), \tag{13}$$

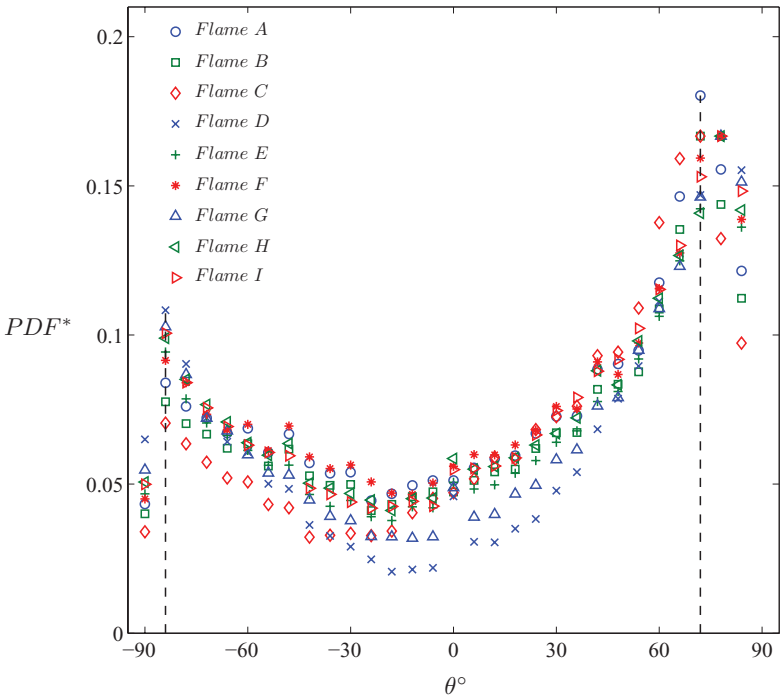

FIG. 19. Probability-density-function of the angle between tangent to the flame front and the x-axis.

where the index i corresponds to the ith point along the flame front. For all experimental conditions tested and for all acquired images, θ was calculated along the right wing of the flame front, with a resolution equal to the inner cutoff scale of the corresponding experimental condition.

For all experimental conditions tested, the normalized probability-density-function of θ features two peaks, as illustrated in Fig. 19. The angles corresponding to the peaks are insensitive to the experimental conditions tested and are centered at $\theta \approx 78^\circ \pm 6^\circ$ and $-84^\circ \pm 6^\circ$. Root-mean-square

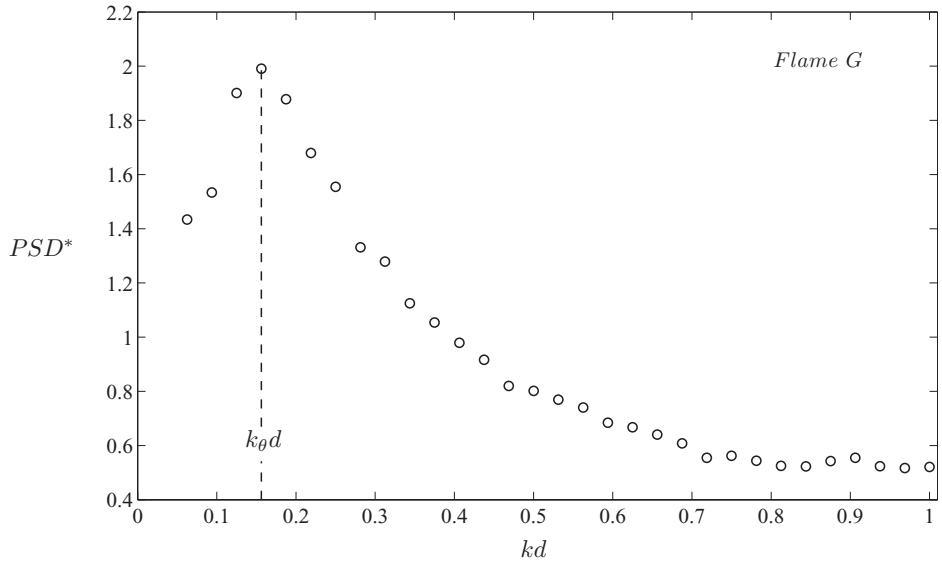

FIG. 20. Power-spectrum-density of the angle between tangent to the flame front and the x-axis. The results correspond to Flame G condition.

of the angle between tangent to the flame front and the x-axis, θ', was estimated. The results show that the values of θ' are independent of the experimental conditions tested and are equal to approximately $60^\circ \pm 3^\circ$.

Power-spectrum-densities of θ were estimated along the right wing of the flame front and for all the images acquired using the Fast-Fourier-Transform technique. The Hanning window function was utilized for all FFT calculations. The PSDs were obtained at 64 points along the flame front. For each experimental condition, the PSDs were averaged over the data obtained from all the images. Then, the results were normalized by the area under the curve of averaged PSD against the wave number. The normalized and averaged power-spectrum-densities pertaining to Flame G is presented in Fig. 20. The results in the figure show that the PSD^* features a peak. The wave number corresponding to the peak is referred to as k_θ. Indeed, for all the experimental conditions tested the power-spectrum-density of the angle between tangent to the flame front and the horizontal axis features a peak. For all the conditions tested, the values of $1/k_\theta$ along with their corresponding uncertainties are tabulated in Table III. The results in the table show that the values of $1/k_\theta$, similar to those of $1/k_c$, are larger than the values of the integral length scale, the flame front wrinkling scale, and $1/\kappa'$. This disagreement suggests that $1/k_\theta$, similar to $1/k_c$, does not provide a realistic length scale for the flame front wrinkles.

IV. CONCLUDING REMARKS

Flame front characteristics of turbulent premixed V-shaped flames were investigated experimentally. A cylindrical wire was used for stabilizing the flames. A perforated plate was utilized to produce turbulence in fresh gases. Three mean streamwise exit velocities: 4.0, 6.2, and 8.6 m/s along with three fuel-air equivalence ratios: 0.7, 0.8, and 0.9 were tested. The Mie scattering and particle image velocimetry techniques were utilized in the experiments. The Mie scattering technique was used to investigate flame front characteristics and the particle image velocimetry technique was used to measure turbulent flow characteristics. Effects of the vertical distance from the flame-holder, the mean streamwise exit velocity, and the fuel-air equivalence ratio on statistics of flame front position, flame brush thickness, flame front curvature, and flame front orientation were studied.

For the lean flame conditions tested, the results show that the mean and RMS of the flame front position increase with increase in the fuel-air equivalence ratio from 0.7 to 0.9. The vertical distance from the flame-holder has a similar effect on the mean and RMS of the flame front position. However, increasing the mean streamwise exit velocity decreases these statistics. For all experimental conditions tested, the probability-density-function of the flame front position has a bell-shaped distribution. Spectral analysis of the flame front position shows that the normalized and averaged power-spectrum-densities collapse for all the experimental conditions tested. For the normalized wave numbers between 0.2 and 1, the normalized and averaged power-spectrum-density has a power-law relation with the normalized wave number. Autocorrelation of the flame front position was used to estimate a length scale associated with the flame front wrinkles. Values of this length scale are close to those of the integral length scale. This means that, for the experimental conditions tested, large turbulent structures play a significant role in wrinkling of the flame front.

The flame brush thickness was estimated using the mean-progress-variable. Analyses of the results associated with the flame brush thickness and the flame front position show that, for all experimental conditions tested and for all vertical distances from the flame-holder, the flame brush thickness is linearly correlated with the RMS of flame front position. Slope of the line is approximately 3.1.

Mean value of the flame front curvature was zero for all the experimental conditions tested. The results show that values of inverse of the RMS of the flame front curvature are similar to those of the integral length scale and the flame front wrinkling scale. For all experimental conditions tested, the PDF of the curvature data shows a bell-shaped distribution. Analysis of the PDF of the curvature data shows that the results are asymmetric with respect to zero. Spectral analysis of the curvature data shows that, for all experimental conditions tested, the power-spectrum-densities feature a peak. Inverse of the wave number at which the peak is centered is larger than the integral length scale of the corresponding experimental condition.

The angle between tangent to the flame front and the horizontal axis was used to investigate the flame front orientation. The probability-density-function of the angle features two peaks. The angles corresponding to the peaks are independent of the experimental conditions tested and are equal to approximately $75^\circ \pm 6^\circ$ and $-84^\circ \pm 6^\circ$. Also, RMS of the angle between tangent to the flame front and the horizontal axis is independent of the experimental conditions tested and equals to approximately $60^\circ \pm 3^\circ$. Spectral analysis of the angle between tangent to the flame front and the horizontal axis shows that the normalized and averaged power-spectrum-densities feature a peak. Inverse of the wave number pertaining to the peak is larger than the integral length scale of the corresponding experimental condition.

ACKNOWLEDGMENTS

The authors are grateful for financial support from the Natural Sciences and Engineering Research Council (NSERC) of Canada.

[1] N. Peters, *Turbulent Combustion*, 1st ed. (Cambridge University Press, 2000).
[2] I. Glassman and R. A. Yetter, *Combustion*, 4th ed. (Elsevier Inc., 2008).
[3] P. Clavin, "Dynamic behavior of premixed flame fronts in laminar and turbulent flows," Prog. Energy Combust. Sci. **11**, 1–59 (1985).
[4] J. F. Driscoll, "Turbulent premixed combustion: Flamelet structure and its effect on turbulent burning velocities," Prog. Energy Combust. Sci. **34**, 91–134 (2008).
[5] A. N. Lipatnikov and J. Chomiak, "Turbulent flame speed and thickness: phenomenology, evaluation, and application in multi-dimensional simulations," Prog. Energy Combust. Sci. **28**, 1–74 (2002).
[6] I. G. Shepherd, G. L. Hubbard, and L. Talbot, "The dynamic structure of turbulent V-shaped premixed flames," Proc. Combust. Inst. **21**, 1377–1383 (1986).
[7] M. Namazian, I. G. Shepherd, and L. Talbot, "Characterization of the density fluctuations in turbulent V-shaped premixed flames," Combust. Flame **64**, 299–308 (1986).
[8] S. Rajan, J. R. Smith, and G. D. Rambach, "Internal structure of a turbulent premixed flame using Rayleigh scattering," Combust. Flame **57**, 95–107 (1984).
[9] D. Veynante, J. M. Duclos, and J. Piana, "Experimental analysis of flamelet models for premixed turbulent combustion," Proc. Combust. Inst. **25**, 1294–1256 (1994).
[10] A. Soika, F. Dinkelacker, and A. Leipertz, "Measurement of the resolved flame structure of turbulent premixed flames with constant Reynolds number and varied stoichiometry," Proc. Combust. Inst. **27**, 798–792 (1998).
[11] A. C. Eckbreth, *Laser Diagnostics for Combustion Temperature and Species*, 2nd ed. (Overseas Publishers Association, 1996).
[12] J. R. Hertzberg, M. Namazian, and L. Talbot, "A laser tomographic study of a laminar flame in a K*árm*á*n* vortex street," Combust. Sci. Technol. **38**, 205–216 (1984).
[13] P. Goix, P. Paranthoen, and M. Trinite, "A tomographic study of measurements in a V-shaped H_2-air flame and a Lagrangian interpretation of the turbulent flame brush evolution," Combust. Flame **81**, 229–241 (1990).
[14] K. Atashkari, M. Lawes, C. G. W. Sheppard, and R. Wolley, "Towards a general correlation of turbulent premixed flame wrinkling," in *Proceedings of the 4th International Symposium on Engineering Turbulence Modelling and Measurements*, edited by W. Rodi and D. Laurence (Engineering Turbulence Modelling and Experiments - 4, 1999), pp. 805–814.
[15] D. C. Bingham, F. C. Gouldin, and D. A. Knaus, "Crossed-plane laser tomography: Direct measurement of the flamelet surface normal," Proc. Combust. Inst. **27**, 77–84 (1998).
[16] J. B. Bell, M. S. Day, I. G. Shepherd, M. R. Johnson, R. K. Cheng, J. F. Grcar, V. E. Beckner, and M. J. Lijewski, "Numerical simulation of a laboratory-scale turbulent V-flame," Proc. Natl. Acad. Sci. U.S.A. **102**, 10006–10011 (2005).
[17] P. C. Miles and F. C. Gouldin, "Mean reaction rates and flamelet statistics for reaction rate modelling in premixed turbulent flames," Proc. Combust. Inst. **24**, 477–484 (1992).
[18] D. A. Knaus and F. C. Gouldin, "Measurements of flamelet orientations in premixed flames with positive and negative Markstein numbers," Proc. Combust. Inst. **28**, 367–373 (2000).
[19] S. S. Sattler, D. A. Knaus, and F. C. Gouldin, "Determination of three-dimensional flamelet orientation distributions in turbulent V-flames from two-dimensional image data," Proc. Combust. Inst. **29**, 1785–1792 (2002).
[20] N. Peters, "Laminar flamelet concepts in turbulent combustion," Proc. Combust. Inst. **21**, 1231–1250 (1986).
[21] G. J. Smallwood, Ö. L. Gülder, D. R. Snelling, B. M. Deschamps, and I. Gökalp, "Characterization of flame front surfaces in turbulent premixed methane/air combustion," Combust. Flame **101**, 461–470 (1995).
[22] Ö. L. Gülder, "Contribution of small scale turbulence to burning velocity of flamelets in the thin reaction zone regime," Proc. Combust. Inst. **31**, 1369–1375 (2007).
[23] F. T. C. Yuen, "Experimental investigation of the dynamics and structure of lean-premixed turbulent combustion," Ph.D. dissertation (University of Toronto Institute for Aerospace Studies, Toronto, ON, Canada, 2009).
[24] P. C. Miles, "Conditional velocity statistics and time-resolved flamelet statistics in premixed turbulent V-shaped flames," Ph.D. dissertation (Cornell University, Ithaca, NY, 1991).
[25] Y.-C. Chen, M. Kim, J. Han, S. Yun, and Y. Yoon, "Analysis of flame surface normal and curvature measured in turbulent premixed stagnation-point flames with crossed-plane tomography," Proc. Combust. Inst. **31**, 1327–1335 (2007).

[26] T. W. Lee, G. L. North, and D. L. Santavicca, "Surface properties of turbulent premixed propane/air flames at various Lewis numbers," Combust. Flame **93**, 445–456 (1993).
[27] W. L. Roberts, J. F. Driscoll, M. C. Drake, and L. P. Goss, "Images of quenching of a flame by a vortex-to quantify regimes of turbulent combustion," Combust. Flame **94**, 58–69 (1993).
[28] G. E. Andrews and D. Bradley, "The burning velocity of methane-air mixtures," Combust. Flame **19**, 275–288 (1972).
[29] J. Jarosinski, "The thickness of laminar flames," Combust. Flame **56**, 337–342 (1984).
[30] S. B. Pope, *Turbulent Flows* (Cambridge University Press, 2000).
[31] J. S. Bendat and A. G. Piersol, *Random Data Analysis and Measurement Procedures*, 2nd ed. (John Wiley & Sons, Inc., 1986).
[32] I. G. Shepherd, "Flame surface density and burning rate in premixed turbulent flames," Proc. Combust. Inst. **26**, 373–379 (1996).
[33] H. Lomax, T. H. Pulliam, and D. W. Zingg, *Fundamentals of Computational Fluid Dynamics* (Springer, 1999).
[34] A. Soika, F. Dinkelacker, and A. Leipertz, "Pressure influence on the flame front curvature of turbulent premixed flames: comparison between experiment and theory," Combust. Flame **132**, 451–462 (2003).
[35] F. T. C. Yuen and Ö. L. Gülder, "Turbulent premixed flame front dynamics and implications for limits of flamelet hypothesis," Proc. Combust. Inst. **34**, 1393–1400 (2013).
[36] D. Veynante, J. Piana, J. M. Duclos, and C. Martel, "Experimental analysis of flame surface density models for premixed turbulent combustion," Proc. Combust. Inst. **26**, 413–420 (1996).